

# Novel Multiferroic Phases and Phenomena in Epitaxial (111) BiFeO<sub>3</sub> Films

Changsong Xu, Hongjun Xiang, and Laurent Bellaiche\*

Multiferroics are attracting much interest because they simultaneously possess ordered electric and magnetic dipoles. In particular, numerous recent studies are devoted to find novel multiferroic phases, as, for example evidenced by the flurry of activities that accompanied the discovery of the so-called T-phase in BiFeO<sub>3</sub> systems, when these latter are made in forms of (001) epitaxial films and subject to high-enough compressive strains. Here it is predicted, via the combined use of a genetic algorithm and first-principles calculations, that novel multiferroic phases, as well as new phenomena, can also occur in epitaxial BiFeO<sub>3</sub> films, but when grown along the less conventional [111] direction and when experiencing large enough tensile strains. One example includes the hexagonal YMnO<sub>3</sub>-type *P6<sub>3</sub>cm* phase, that exhibits an anomalous behavior for its out-of-plane electric polarization and that can also undergo magnetic transitions when varying the tensile strain. Another striking example is the emergence of an unusual crystal structure of triclinic symmetry, that possesses controllable polarization's direction as well as magnetic spiral structures whose characteristics (e.g., periodicity and propagation direction) can be altered by epitaxial strain. Such findings may open new ways to design multiferroics and novel devices exploiting their cross-coupling between electric and magnetic properties.

## 1. Introduction

Multiferroic materials exhibit a coexistence of electric polarization and magnetic ordering, with these two quantities being coupled via the magnetoelectric effect.<sup>[1,2]</sup> As such, it has long been expected that they will lead to a breakthrough in spintronics and memory devices.<sup>[3–8]</sup> However, multiferroic compounds and phases are rather rare in nature, and so far exhibit disadvantages that prevent their use in technologies.

Dr. C. Xu, Prof. H. Xiang, Prof. L. Bellaiche  
 Physics Department and Institute for Nanoscience and Engineering  
 University of Arkansas  
 Fayetteville, AR 72701, USA  
 E-mail: laurent@uark.edu

Prof. H. Xiang  
 Key Laboratory of Computational Physical Sciences  
 (Ministry of Education)  
 State Key Laboratory of Surface Physics  
 and Department of Physics  
 Fudan University  
 Shanghai 200433, China

 The ORCID identification number(s) for the author(s) of this article can be found under <https://doi.org/10.1002/aelm.201700332>.

DOI: 10.1002/aelm.201700332

For example, bismuth ferrite (BiFeO<sub>3</sub> or BFO) perovskite, which is likely the most studied multiferroic system to date because of its large polarization and high ordering temperatures,<sup>[9,10]</sup> has a relatively weak magnetoelectric coupling in its bulk form<sup>[11]</sup> (which adopts the so-called R-phase<sup>[12]</sup>), which hinders its technical application. Similarly, the other intensively studied class of multiferroics formed by hexagonal *Re*MnO<sub>3</sub> and *Re*FeO<sub>3</sub> materials, where *Re* is a rare-earth or the Y ion (see, e.g., refs. [13] and [14] and references therein), has a relatively small value for their out-of-plane polarization (e.g.,  $\approx 6 \mu\text{C cm}^{-2}$  in YMnO<sub>3</sub><sup>[15,16]</sup>) due to their improper character, which may be a disadvantage to their utilization in devices.

As a result, searching for novel multiferroic materials or even novel phases in already known multiferroics constitutes an active research activity.<sup>[12,17–23]</sup> For instance, the discovery of a novel multiferroic phase, the so-called T-phase, in BFO systems grown as thin films along the pseudocubic [001] direction and under large compressive

strain<sup>[12,24]</sup> has generated a large interest, especially since large magnetoelectric effects have been predicted to occur near the strain-induced boundary between the R and T phases.<sup>[25,26]</sup> Based on the aforementioned findings and the fact that paraelectric magnetic perovskites made of *Re*FeO<sub>3</sub> have been recently predicted to transform into polar hexagonal YMnO<sub>3</sub>-type phases (and thus to become multiferroic) when grown on top of (111) cubic or (0001) hexagonal substrates exercising a large enough tensile strain,<sup>[27]</sup> it is legitimate to wonder if such latter, rather atypical for now, conditions of growth and epitaxial strain can also give rise to novel multiferroic phases and effects in BFO films.

The goal of this paper is to reveal that epitaxial (111) BiFeO<sub>3</sub> films are indeed predicted to adopt new multiferroic phases when placed under large enough tensile strain. For instance, they can exhibit not only the polar hexagonal YMnO<sub>3</sub>-type configuration but also another brand new crystal structure of triclinic symmetry. These hexagonal and triclinic states are further numerically found to display unusual properties, such as an out-of-plane polarization anomalously increasing when increasing tensile epitaxial strain (due to the appearance of a proper ferroelectric character) and an electrically controllable spiral magnetism, respectively. In particular, the presently determined triclinic structure appears to be rather promising to induce strong or novel magnetoelectric effects, due to the fact

that both its in-plane polarization and magnetism are inherently coupled to the same specific Fe–O bond.

## 2. Results and Discussion

As indicated in the Experimental Section and the Supporting Information, *ab initio* calculations are performed on different structural phases of BFO films. Six selected phases that are subjected to tensile epitaxial strain are represented in Figure 1a–c,e,f. Three of them (namely, *R3c*, *Cc-I*, and *Cc-II*) crystallize in the perovskite structure and are grown along their pseudocubic [111] direction, which can be practically accomplished by using cubic (111) or hexagonal (0001) substrates—as schematized in Figure 1d and described in ref. [28]. The out-of-plane direction of the remaining three states (that are *P6<sub>3</sub>cm*, *P3c1*, and a phase we coined here as “hex-like” *P1*) is basically along the hexagonal [0001] axis, which can also be made possible by growing them on cubic (111) substrates (such as yttrium stabilized zirconium oxide (YSZ)), or hexagonal (0001) substrates (e.g., Cr<sub>2</sub>O<sub>3</sub> and Fe<sub>2</sub>O<sub>3</sub>).<sup>[28,29]</sup> We now discuss in detail these phases, including their properties and stability ranges.

### 2.1. Perovskite Phases

For small tensile strains, our computations predict that epitaxial (111) BFO films adopt the rhombohedral *R3c* structure with a polarization being fully out-of-plane, which is consistent with the fact that this structure is the known ground state of BFO

bulks.<sup>[3,30]</sup> In particular and as shown in Figure 2a,b, the *R3c* phase at equilibrium (i.e., when the in-plane epitaxial strain is zero) is numerically found to have an in-plane lattice parameter  $a_{1P} = 5.550$  Å and an out-of-plane lattice constant  $c_{\text{hex}} = 13.699$  Å in an hexagonal basis (which correspond to  $a = b = c = 5.578$  Å and  $\alpha = \beta = \gamma = 59.664^\circ$  in the rhombohedral setting). Our calculated values therefore yield a rather small and reasonable underestimation of  $-0.48\%$  and  $-1.2\%$ , when compared with the measured  $a_{1P} = 5.577$  Å and  $c_{\text{hex}} = 13.867$  Å of refs. [3] and [31], respectively.

Moreover, Figure 2a reveals that these (111) BFO films transform into a *Cc-I* phase when the epitaxial tensile strain reaches  $0.92\%$  ( $a_{1P} = 5.601$  Å). Such phase has an out-of-plane lattice constant  $c = 7.840$  Å and an  $\alpha$  angle of  $35.094^\circ$  for the critical strain of  $0.92\%$ , with this  $c$  parameter slightly increasing while the  $\alpha$  angle decreases when the strain further increases. Then, when the strain reaches  $7.2\%$  ( $a_{1P} = 5.950$  Å), BFO films further transform into another monoclinic phase with the same *Cc* space group, that is the *Cc-II* state. In other words, these BFO films undergo an isostructural phase transition. Note that *Cc-II* differs, in particular, from *Cc-I* by a longer  $c$ -axis and a smaller  $\alpha$  angle, as shown in Figure 2b,c. To the best of our knowledge, those *Cc-I* and *Cc-II* phases have never been reported in any epitaxial (111) perovskite film.

### 2.2. Hexagonal *P6<sub>3</sub>cm* Phase

As further indicated in the phase diagram of Figure 2a, the YMnO<sub>3</sub>-type phase, which is of *P6<sub>3</sub>cm* symmetry and thus

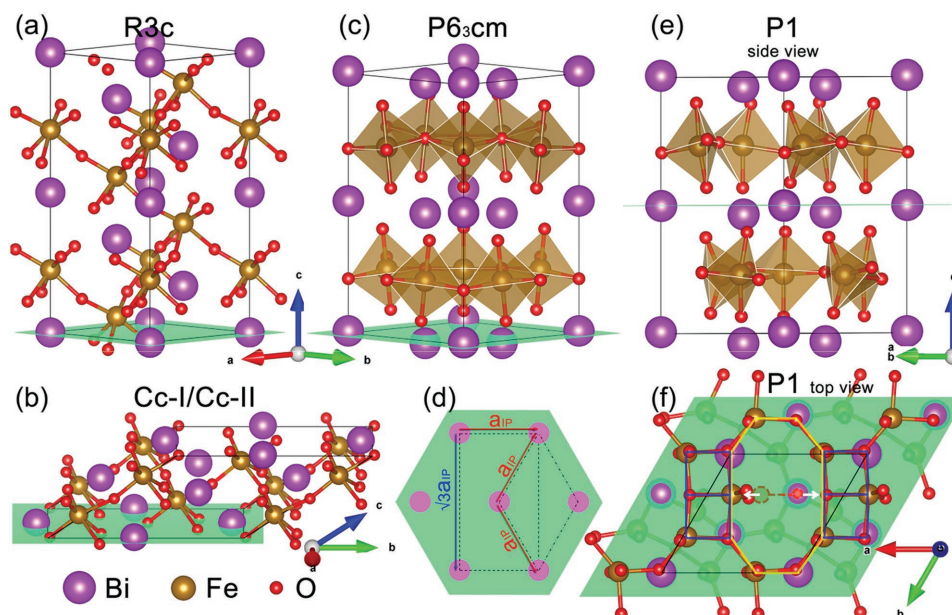


**Figure 1.** Considered phases and corresponding basal planes. Panels a) and b) display the *R3c* and *Cc-I/Cc-II* phases, respectively, within the perovskite crystal structure. Panel c) shows the hexagonal *P6<sub>3</sub>cm* phase. Panels e) and f) are the side and top views of the hex-like *P1* phase. Panel d) schematizes the matching mechanism of the considered phases grown on cubic (111) or hexagonal (0001) substrates. The green planes shown in different panels represent the substrate plane. The FeO<sub>5</sub> trigonal bipyramids indicated in the text are depicted in panels (c) and (e). In panel (f), the dashed circles mark the positions of the specific Fe and O ions mentioned in the paper in the high symmetry *P6<sub>3</sub>/mmc* phase and the white arrows depict the directions in which these ions displace in the hex-like *P1* phase. Solid blue and yellow lines of panel (f) indicate the small “8-shaped” Fe–O structure and the large Fe–O ring, respectively, in this hex-like *P1* phase.

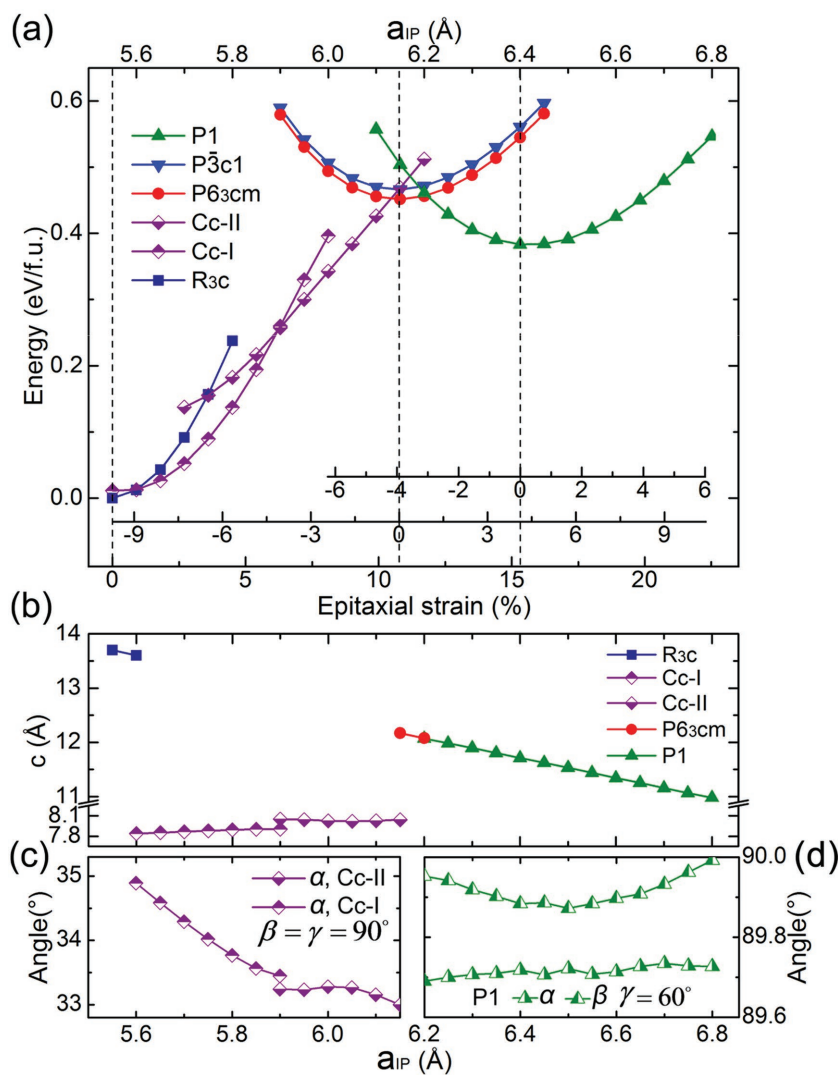


**Figure 2.** Phase diagram and lattice parameters. Panel a), energy-versus-tensile strain phase diagram of BFO films when grown on cubic (111) or hexagonal (0001) substrates. The bottom axes indicate the epitaxial strain, as calculated from three different choices of the origin (namely, with respect to the minimum of energy of the R3c,  $P6_3cm$ , or hex-like P1 phase), while the top axis shows the in-plane lattice constant  $a_{IP}$ . Panel b), out-of-plane lattice parameter  $c$  of considered phases. Panel c),  $\alpha$  angle of the Cc-I and Cc-II phases. Panel d),  $\alpha$  and  $\beta$  angles of the hex-like P1 phase.

hexagonal and polar, becomes the ground state of our investigated epitaxial BFO films, for  $a_{IP}$  ranging between 6.13 and 6.21 Å. Such range of lattice constants strongly suggests that it is possible to experimentally observe for the first time hexagonal BFO films by growing them on a rhombohedral  $Cr_2O_3$  (0001) substrate, since this latter system has an effective lattice constant of 6.19 Å.<sup>[28,29]</sup> The observation of the  $P6_3cm$  phase of BFO should be feasible even if the corresponding strain (with respect to BFO bulk) is larger than 10% because this phase is a polymorph form of BFO, in the same manner than the so-called T-like state was experimentally seen in (001) BFO films for compressive strains being larger than 7% in magnitude.<sup>[12,24]</sup> Note that Figure 2a also indicates that the polar  $P6_3cm$  phase is always  $\approx 15$  meV f.u.<sup>-1</sup> lower in energy than the nonpolar hexagonal  $P\bar{3}c1$  phase within the investigated range extending from  $a_{IP} = 5.90$  to 6.45 Å, and adopts its minimum energy for  $a_{IP} = 6.144$  Å.

Furthermore, Figure 3a displays the dependency of the polarization of  $P6_3cm$  (which is oriented along the out-of-plane  $c$ -axis) on the in-plane lattice parameter. We cover here a range of  $a_{IP}$  that is much larger than the stability window over which the  $P6_3cm$  phase is the ground state, in order to better appreciate such dependency. Figure 3a shows that this polarization changes from  $6.24 \mu C cm^{-2}$  for  $a_{IP} = 6.0$  Å to  $9.82 \mu C cm^{-2}$  for  $a_{IP} = 6.40$  Å, that is it increases by about 57.4%. Such enhancement is rather surprising and original when realizing that the (out-of-plane) polarization of hexagonal rare-earth manganites<sup>[32]</sup> and ferrites<sup>[28]</sup> have been reported to decrease, rather than increase, with tensile strain. To shed more light into such unusual evolution of the polarization in the  $P6_3cm$  phase of BFO, Figure 3b reports the behavior of different phonon modes of this state as a function of  $a_{IP}$ . These modes are (1) the  $K_3$  mode, which is a tilting, soft mode that is known to induce the phase transition from paraelectric  $P6_3/mmc$  to ferroelectric  $P6_3cm$  in hexagonal rare-earth manganites and ferrites,<sup>[13,14]</sup> (2) the  $\Gamma_2^-$  mode, which is related to the polarization of the  $P6_3cm$  phase; and (3) the  $K_1$  and  $\Gamma_1^+$  modes, which also condense in  $P6_3cm$  phases while being usually small in magnitude.<sup>[13,14]</sup> Figure 3b not only shows that  $K_1$  and  $\Gamma_1^+$  are also weak in the  $P6_3cm$  state of BFO but also indicates that the  $K_3$  and  $\Gamma_2^-$  modes differently respond to a change in in-plane lattice constants: the magnitude of the  $K_3$  mode decreases with increasing  $a_{IP}$ , as analogous to what was found in rare-earth manganites  $ReMnO_3$ ,<sup>[32]</sup> while the strength of  $\Gamma_2^-$  is enhanced meanwhile—as consistent with the concomitant increase of polarization displayed in Figure 3a (note that we also numerically found that the out-of-plane component of the Born effective charge (in paraelectric  $P6_3/mmc$  phase) of Bi

increases from 3.86 at  $a_{IP} = 6.10$  Å to 4.40 at  $a_{IP} = 6.40$  Å, which altogether with the enhanced strength of the  $\Gamma_2^-$  mode, leads to the relatively large enhancement of polarization depicted in Figure 3a). To understand such opposite behaviors, Figure 3c further shows the energy associated with the  $\Gamma_2^-$  (respectively,  $K_3$ ) mode as a function of the  $\Gamma_2^-$  (respectively,  $K_3$ ) mode distortion for two different  $a_{IP}$  values, namely,  $a_{IP} = 6.1$  Å versus  $a_{IP} = 6.4$  Å. For the smaller  $a_{IP}$ , the energy associated with  $K_3$  exhibits a double well with the corresponding two minima occurring for nonzero and opposite distortions of the  $K_3$  mode, whereas the energy solely related to  $\Gamma_2^-$  has a single well that is located at the vanishing strength of the  $\Gamma_2^-$  mode. Such features along with Figure 3a reveal the improper nature of the ferroelectricity of hexagonal  $P6_3cm$  phase at smaller in-plane lattice constants. On the other hand, for the larger  $a_{IP} = 6.4$  Å, the double well associated with  $K_3$  becomes shallower, which attests

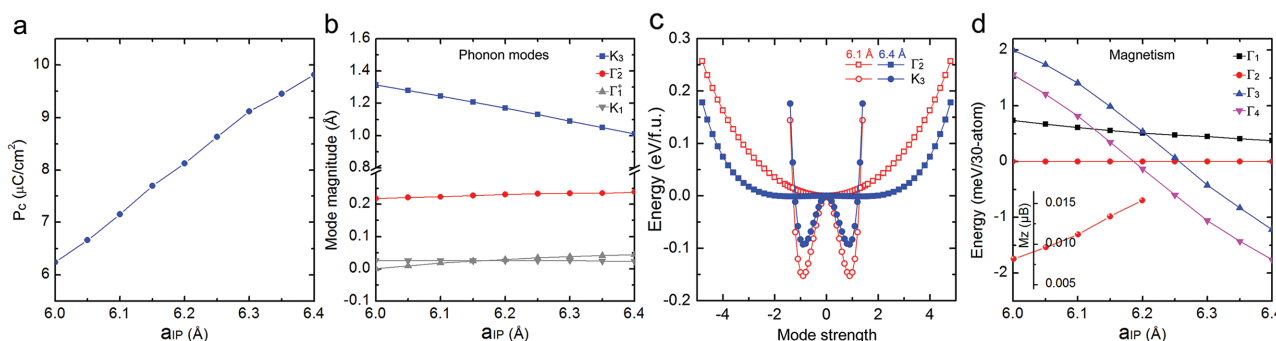


**Figure 3.** Ferroelectric, structural and magnetic properties of BiFeO<sub>3</sub> films in their *P*<sub>6<sub>3</sub>*cm*</sub> phase, when grown on cubic (111) or hexagonal (0001) substrates. Panel a), the out of plane polarization  $P_c$  as a function of  $a_{IP}$ . Panel b), the magnitudes of phonon modes  $K_3$ ,  $\Gamma_2^-$ ,  $\Gamma_1^+$ , and  $K_1$ , as a function of  $a_{IP}$ . Panel c), energy associated with the  $\Gamma_2^-$  and  $K_3$  modes at  $a_{IP} = 6.1$  and  $6.4$  Å, with the mode strength of 1 (or  $-1$ ) being the actual strength of these two modes in the *P*<sub>6<sub>3</sub>*cm*</sub> phase. Panel d), energies of  $\Gamma_1$ ,  $\Gamma_2$ ,  $\Gamma_3$ , and  $\Gamma_4$  noncollinear magnetic configurations, as a function of  $a_{IP}$ . The inset of panel (d) shows the weak ferromagnetism associated with  $\Gamma_2$ .

that  $K_3$  is weakened at larger in-plane lattice constants (as consistent with Figure 3b). At the same time, the energy related to  $\Gamma_2^-$  is less “stiff” with respect to the case of  $a_{IP} = 6.1$  Å and can even adopt a (shallow) double well. The enhancement of the  $\Gamma_2^-$  mode amplitude displayed in Figure 3b for larger  $a_{IP}$  therefore originates from (i) this decrease in stiffness, that affects the improper part of the polarization resulting from the coupling between  $\Gamma_2^-$  and  $K_3$ ; and (ii) the possibility that the polarization in the *P*<sub>6<sub>3</sub>*cm*</sub> phase of BFO can acquire a proper character at larger in-plane lattice constants, as consistent with the double well of the energy related to  $\Gamma_2^-$  for  $a_{IP} = 6.4$  Å. Note that the Supporting Information (1) further confirms the acquisition of a proper character of this polarization for large in-plane lattice constants by showing in Figure S4 of the Supporting Information the same energy curves as in Figure 3c but for an even larger  $a_{IP}$  of 6.6 Å; and (2) provides a tight-binding model, based on the hybridization between the 6p<sub>z</sub> orbitals of Bi and the 2p<sub>z</sub> orbitals of O, to explain the occurrence of such proper component.

Regarding magnetism and as indicated in the Experimental Section, four different noncollinear magnetic configurations ( $\Gamma_1$ ,  $\Gamma_2$ ,  $\Gamma_3$ , and  $\Gamma_4$ ) are considered here. They are typical spin arrangements for hexagonal systems, see, e.g., ref. [14]. As shown in Figure 3d, our calculations indicate that the magnetic ground state is  $\Gamma_2$  for  $a_{IP}$  ranging between 6.0 and  $\approx 6.2$  Å, with a corresponding weak, spin–orbit-induced ferromagnetism along the [0001] direction slightly increasing from 0.008 to 0.013  $\mu_B$  per 30 atoms in this interval. On the other hand, the ground state becomes  $\Gamma_4$  for larger  $a_{IP}$ , resulting in a vanishing of weak ferromagnetism. Our computations therefore predict that, within the predicted stability range of the *P*<sub>6<sub>3</sub>*cm*</sub> phase of epitaxial BFO films (i.e., between 6.13 and 6.21 Å), this phase is mainly polar with a weak ferromagnetism but also undergoes a magnetic phase transition at the right border of this stability region (while continuing to be polar with an even larger polarization).

### 2.3. Hex-like *P*1 Phase

Figure 2a further shows that another phase becomes the ground state when  $a_{IP}$  is larger than 6.21 Å. Such phase adopts

the *P*1 space group and is thus triclinic with no symmetry element (except for the trivial identity). It reaches its minimum energy when the in-plane lattice constant is equal to 6.40 Å, and is numerically found to be dynamically stable (i.e., there are no unstable phonons)—as evidenced in Figure S3 of the Supporting Information. Possible substrates that can be experimentally used to confirm our prediction of such novel polymorphic *P*1 phase of BFO are rhombohedral (0001) Fe<sub>2</sub>O<sub>3</sub> (for which the effective lattice constant is 6.30 Å) or (111) YSZ substrate (that possesses an effective lattice constant of 6.32 Å).<sup>[29]</sup>

This *P*1 phase has 30 atoms in its unit cell, as identical to the *P*<sub>6<sub>3</sub>*cm*</sub> state. When relaxing all degrees of freedom (i.e., all lattice vectors and internal atomic positions), we numerically found that the equilibrium *P*1 phase exhibits the following structural parameters:  $a = 6.400$  Å,  $b = 6.403$  Å,  $c = 11.692$  Å,  $\alpha = 89.86^\circ$ ,  $\beta = 89.73^\circ$ , and  $\gamma = 60.36^\circ$ . On the other hand, when simulating the growth of epitaxial BFO films on cubic (111) or hexagonal (0001) substrates, the  $a$  and  $b$  parameters are confined to be the same and the  $\gamma$  angle between them is restricted to be precisely  $60^\circ$ . In that case, the  $\alpha$  and  $\beta$  angles can relax and Figure 2d reveals that they only slightly deviate by less than  $0.3^\circ$  from the ideal  $90^\circ$  angle of hexagonal phases (such as *P*<sub>6<sub>3</sub>*cm*</sub>), within the investigated  $a_{IP}$  range. It is also interesting to realize that the  $c$  parameter of this *P*1 phase is basically identical to that of the *P*<sub>6<sub>3</sub>*cm*</sub> phase when  $a_{IP} = 6.20$  Å, and that these two  $c$  parameters both decrease as the tensile strain increases (see Figure 2b). Because of all these facts related to angles and lattice parameters, one can consider this discovered *P*1 to be derived from a hexagonal structure. That is why we presently refer it as “hex-like *P*1.” This notation also allows to distinguish it from another *P*1 phase sometimes found in perovskites.<sup>[33]</sup> Note that we are not aware that our presently discovered “hex-like *P*1” has ever been previously reported in any ABO<sub>3</sub> material.

Structural similarities between the *P*<sub>6<sub>3</sub>*cm*</sub> and the hex-like *P*1 phases can also be seen by comparing the side view of these two structures shown in Figure 1c,e, respectively. As a matter of fact, in any (0001) Bi layer, both phases adopt a ratio of 1:2 between Bi layers moving up and down along the  $c$ -axis with respect to the Bi plane of the *P*<sub>6<sub>3</sub>*mmc*</sub> paraelectric phase, respectively. Note that this ratio of 1:2 gives rise to a



(ferrielectric) polarization being antiparallel to the  $c$ -axis, and that there is another hex-like  $P1$  state with the same energy but having a polarization being parallel to this  $c$ -axis. In this other state, the ratio between the Bi layers moving up and down along the  $c$ -axis is 2:1 rather than 1:2. On the other hand, major differences also exist between hex-like  $P1$  and  $P6_3cm$  phases. More precisely, while both states possess, in any (0001) Fe layer, iron ions that each bond with two topical O and three equatorial O ions, the resulting  $\text{FeO}_5$  bipyramids displayed in Figure 1c,e are rather different between the two structures. As a matter of fact, in  $P6_3cm$ , these bipyramids tilt (as a consequence of the  $K_3$  mode) and only slightly distort. On the other hand, in hex-like  $P1$ , these bipyramids not only tilt but also significantly distort. This distortion is caused by the opposite motion (with respect to the  $P6_3/mmc$  atomic positions) of some specific Fe ions and one of their bonded equatorial O ions, as schematized in Figure 1f by means of arrows. These opposite motions result in the breaking of the bond between these Fe and O ions and the formation of a new bond between these Fe ions and another of their neighboring O ions. Such displacements lead, in the hex-like  $P1$  state, to the emergence of large Fe–O rings that are indicated by yellow solid lines in Figure 1f, and the creation of smaller “8-shaped” Fe–O structures that are highlighted by means of blue solid lines in Figure 1f. Note that these opposite motions occur along the  $a$ -axis in the top (0001) FeO layer of Figure 1e while they happen along the  $b$ -axis in the bottom (0001) FeO layer of Figure 1e, which make the 8-shaped structures rotating by an angle of  $60^\circ$  when going from one (0001) FeO layer to the adjacent one. Interestingly and as we will emphasize later, these motions along the  $a$ -axis and  $b$ -axis can differ in magnitude, which is also consistent with the triclinic symmetry adopted by the hex-like  $P1$  state. These motions are also responsible for the formation of an in-plane polarization in hex-like  $P1$ , in addition to its out-of-plane component.

Interestingly, each aforementioned specific Fe ion equally bonds with its three different equatorial O ions in the high symmetry  $P6_3/mmc$  phase, and the breaking of any of these three Fe–O bonds results in a low symmetry hex-like  $P1$  phase having the same energy. As a consequence, each polar hex-like  $P1$  phase has three equivalent states that are energetically degenerate, and that can be deduced from each other by

a rotation via  $120^\circ$  about the [0001] axis. Moreover and as indicated above, having a ratio of 1:2 or 2:1 between the (0001) Bi planes moving up and down along the  $c$ -axis of the  $P6_3/mmc$  paraelectric phase provide two different hex-like  $P1$  states having identical energy. One can therefore assert that the hex-like  $P1$  phase is six times degenerate, as a result of the possibility of having three different directions for its in-plane polarization and two opposite values for its out-of-plane polarization. Going from one of such six minima to any other one should be feasible by applying electric fields having specific in-plane and/or out-of-plane components. Note that the existence of these six degenerate minima bears resemblance with the formation of the so-called  $Z_m \times Z_n$  domains found in  $P6_3cm$  phases<sup>[34,35]</sup> when choosing  $n = 3$  (in-plane degeneracy) and  $m = 2$  (out-of-plane degeneracy).

Let us now concentrate on the out-of-plane component of hex-like  $P1$ , to be denoted as  $P_c$ . Figure 4a indicates that  $P_c$  is negative for our chosen hex-like  $P1$  state (that is, it lies antiparallel to the  $c$ -axis), is nearly constant and equal to  $-8.1 \mu\text{C cm}^{-2}$  when  $a_{\text{IP}}$  ranges between 6.20 and 6.30 Å, before decreasing in magnitude when  $a_{\text{IP}}$  is larger than 6.35 Å. Moreover and as indicated above, the hex-like  $P1$  also has an in-plane polarization, which contrasts with the case of  $P6_3cm$ . The very low-symmetry of hex-like  $P1$  further allows it to make the components of this in-plane polarization along the  $a$  and  $b$  axes (to be coined  $P_a$  and  $P_b$ , respectively) different from each other. The origin of  $P_a$  and  $P_b$  in our chosen hex-like  $P1$  state can be traced back to the aforementioned motions of specific Fe and O ions along the  $a$ -axis in one type of (0001) FeO layers versus the  $b$ -axis in the second type of (0001) FeO layers, which results in the formation of Fe–O bonds to be denoted as  $d_{\text{Fe-O}}^a$  and  $d_{\text{Fe-O}}^b$ , respectively. These two types of bonds are further shown in Figure 4b and are not equal to each other in magnitude within the same hex-like  $P1$  structure, which is consistent with the fact that  $P_a$  and  $P_b$  can differ from each other. We also found that  $d_{\text{Fe-O}}^a$  and  $d_{\text{Fe-O}}^b$  can vary with  $a_{\text{IP}}$ , which suggests that one can tune the magnitude but also direction of the in-plane polarization by epitaxial strain. To check such exciting possibility, Figure 4a further reports  $P_a$  and  $P_b$ , as a function of  $a_{\text{IP}}$ . When the in-plane lattice parameter is equal to 6.20 Å,  $P_a$  and  $P_b$  are close to each other and equal to  $9.3 \mu\text{C cm}^{-2}$  in our selected hex-like  $P1$  state.

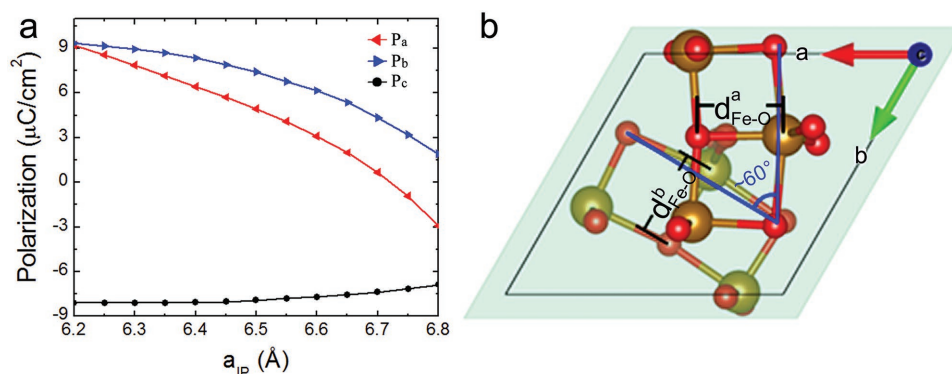


**Figure 4.** Structural and ferroelectric properties of the hex-like  $P1$  phase in  $\text{BiFeO}_3$  films grown on cubic (111) or hexagonal (0001) substrates. Panel a) shows the polarization components  $P_a$ ,  $P_b$ , and  $P_c$ , as a function of  $a_{\text{IP}}$ . Panel b) shows the top view of the hex- $P1$  phase, indicating only Fe and O atoms and with the axes being shown on the top right. Panel (b) also displays the  $d_{\text{Fe-O}}^a$  and  $d_{\text{Fe-O}}^b$  bond lengths in the top and the bottom (0001) FeO layers, respectively.

This gives rise to an in-plane polarization having a magnitude of  $16.1 \mu\text{C cm}^{-2}$  and being oriented along the  $\mathbf{a} + \mathbf{b}$  direction. Considering the triple in-plane degeneracy, the two other in-plane polarizations that hex-like  $P1$  states can possess are oriented along  $\mathbf{a} - 2\mathbf{b}$  and  $-2\mathbf{a} + \mathbf{b}$ , respectively, for  $a_{\text{IP}} = 6.20 \text{ \AA}$ . On the other hand, for  $a_{\text{IP}} = 6.80 \text{ \AA}$ ,  $P_a$  becomes negative, with a value close to  $-3 \mu\text{C cm}^{-2}$ , which is opposite in sign and about twice as larger in magnitude than  $P_b$ . As a result, the in-plane polarization has now a magnitude of  $2.57 \mu\text{C cm}^{-2}$  and lies along the direction spanned by  $-2\mathbf{a} + \mathbf{b}$  direction. Correspondingly, the other two degenerate in-plane polarization are now lying along  $\mathbf{a} + \mathbf{b}$  and  $\mathbf{a} - 2\mathbf{b}$ , respectively. Figure 4a therefore shows that the in-plane polarization can rotate and typically decreases in magnitude, when varying  $a_{\text{IP}}$  from 6.20 to 6.80  $\text{\AA}$ .

Let us now concentrate on magnetism in this hex-like  $P1$  phase. We compute the Heisenberg coupling coefficients  $J$  between any two Fe ions that are connected to each other via an O ion, for a chosen hex-like  $P1$  state (out of the six degenerate ones). All couplings are numerically found to be antiferromagnetic (AFM) in nature and their magnitudes are mainly related to the Fe–O–Fe bond angle, that is the closer this angle is to  $180^\circ$ , the larger is the  $J$  coefficient. The strongest coupling is between the Fe ions denoted as Fe2 and Fe3 in Figure 5a,b, and is thus coined here  $J_{23}$ . The second strongest are the ones denoted as  $J_{23'}$  and  $J_{23}$ , followed by the ones coined  $J_{12'}$  and  $J_{13'}$ . The weakest couplings among all considered here are the ones denoted as  $J_{12}$  and  $J_{13}$ , and therefore involve Fe1 ions. Interestingly, Fe1 ions are the aforementioned specific Fe ions that are responsible for the formation of the in-plane polarization in hex-like  $P1$  and that form the bonds denoted as  $d_{\text{Fe-O}}^a$  and  $d_{\text{Fe-O}}^b$  in Figure 4b. Note also that Fe2' ions can be reached from Fe2 ions via a translation by  $-\mathbf{b}$  in the top layer or by  $\mathbf{a} - \mathbf{b}$  in the bottom layer. They are thus structurally equivalent ions belonging to different adjacent unit cells, and magnetically couple in a different

quantitative way with the Fe1 ions. Similarly, Fe3 and Fe3' are structurally equivalent ions belonging to neighboring unit cells. Note that, despite the fact we use the same notations (of Fe1, Fe2, Fe2', Fe3, or Fe3') for Fe ions belonging to different (0001) planes, the magnetic coupling coefficients are slightly different between the top and the bottom (0001) FeO layers because the corresponding Fe–O–Fe bond angles can differ between these two layers. As shown in Figure 5d, we practically computed all these  $J$  coefficients for four different values of  $a_{\text{IP}}$ , namely, 6.25, 6.45, 6.60, and 6.80  $\text{\AA}$ . The four medium strength couplings,  $J_{12'}$ ,  $J_{13'}$ ,  $J_{23'}$ , and  $J_{23}$ , continuously decrease by about 3 meV from  $a_{\text{IP}} = 6.25$  to 6.80  $\text{\AA}$ , while the weakest  $J_{12}$  and  $J_{13}$  only slightly vary with the in-plane lattice parameters. On the other hand,  $J_{23}$ , which continues to be the strongest coupling, first decreases from 10.97 to 9.76 meV in the top layer (from 9.65 to 8.92 meV in the bottom layer, respectively), then reaches a minimum at  $a_{\text{IP}} = 6.60 \text{ \AA}$  and then increases up to 10.69 meV (10.06 meV, respectively) when  $a_{\text{IP}}$  from 6.25 to 6.80  $\text{\AA}$ .

We then ran Monte Carlo calculations<sup>[17]</sup> with these coupling coefficients on  $n \times n \times 1$  supercells with  $n$  varying from 1 to 20 (note that the dimension of 1 along the  $c$ -axis implies that our chosen supercells contain both the top and the bottom (0001) FeO layers of Figure 1e), and computed the total magnetic energy (see Figure 5e) in order to find the magnetic ground state. Strikingly, this latter yields a spiral structure, an example of which is shown in Figure 5c for  $a_{\text{IP}} = 6.45 \text{ \AA}$ . In that case, this spiral structure propagates along the  $b$ -axis in the top (0001) FeO layer of Figure 1e, while it is along the  $a$ -axis in the bottom (0001) FeO layer, with a periodicity of nine unit cells (which corresponds to a distance of 58.05  $\text{\AA}$ ). On the other hand, the spins adopt the same direction when moving along the  $a$ -axis (respectively,  $b$ -axis) in the top (respectively, bottom) FeO layer. Note that the periodicity of nine unit cells found for  $a_{\text{IP}} = 6.45 \text{ \AA}$  implies that the angle between any two adjacent

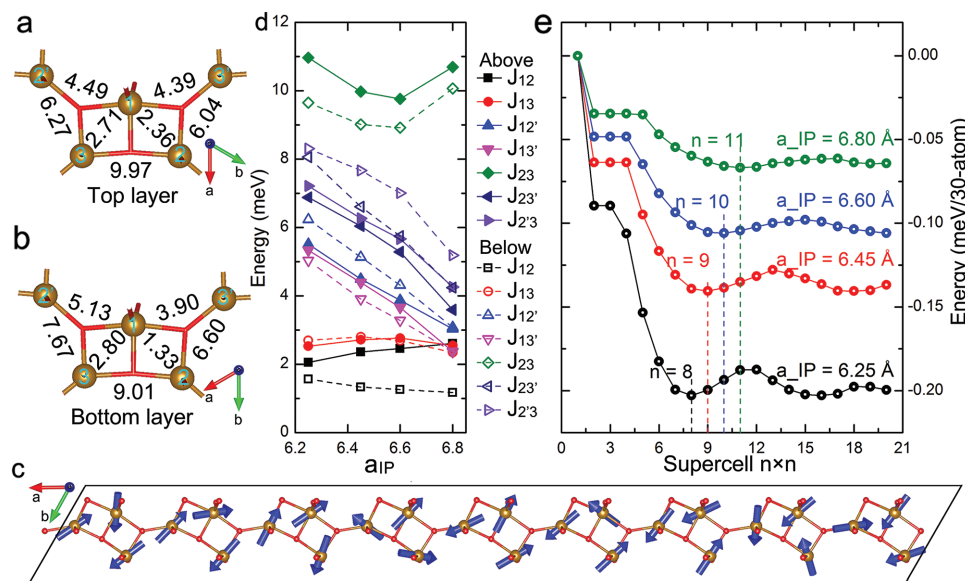


**Figure 5.** Magnetic properties of the hex-like  $P1$  phase. Panels a) and b) show the coupling exchange coefficients  $J$  (in unit of meV) between Fe ions, in the top and the bottom (0001) FeO layers, respectively, for  $a_{\text{IP}} = 6.45 \text{ \AA}$ . Panel c) displays the spiral magnetic pattern (for the bottom (0001) FeO layer, as an example) at  $a_{\text{IP}} = 6.45 \text{ \AA}$ . Panel d) provides the coupling coefficients as a function of  $a_{\text{IP}}$ . Panel (e) gives the magnetic energy as a function of the supercell size at different  $a_{\text{IP}}$ . Note that the spiral period corresponds to the energy minimum for any chosen  $a_{\text{IP}}$ .

spins in that spiral is  $40^\circ$ , with these rotations resulting in a zero net magnetization. It is important to realize that such spin spiral results solely from Heisenberg interactions and is thus due to the specific crystal structure and the AFM frustration, since we did not incorporate spin–orbital coupling and inter-layer couplings in our computations (because they are typically much weaker than AFM exchange couplings<sup>[14]</sup>). The correlation between the crystal structure and the magnetic spiral configuration is further emphasized by the facts that the spiral is numerically found to change its periodicity, but not its propagation direction, when varying the in-plane lattice parameter: as shown in Figure 5e, MC simulations indicate that the spiral period increases from  $n = 8$  at  $a_{\text{IP}} = 6.25 \text{ \AA}$  to  $n = 11$  at  $a_{\text{IP}} = 6.80 \text{ \AA}$ . Such sensitivity, altogether with the strong dependence of the in-plane polarization with  $a_{\text{IP}}$  shown in Figure 4a, hints toward a strong magnetoelectric coupling in any degenerate hex-*P1* state of BFO. Moreover, it is important to emphasize that our simulations show (see Figure 5c) that, in each of the two different (0001) FeO layers, the direction of propagation forms an angle of about  $60^\circ$  from the aforementioned specific Fe–O bond, that is  $d_{\text{Fe–O}}^a$  in the top (0001) FeO layer and  $d_{\text{Fe–O}}^b$  in the bottom (0001) FeO layer. As a result, applying an electric field and switching the in-plane polarization by  $120^\circ$  among the aforementioned three degenerate states having different direction for their in-plane polarization should result in the change of the propagation direction of the magnetic spiral pattern by  $120^\circ$  as well (note that the  $J$  parameters between the same Fe ions are dependent on the direction of the displacement of Fe1 ion, and thus change from one degenerate state to another, as schematized in Figure S6, Supporting Information). This control of the propagation direction of the magnetic spirals by an electric field therefore constitutes an original magnetoelectric effect. Interestingly and unlike the case of the magnetic cycloid of bulk BFO (in its perovskite *R3c* state),<sup>[4,36–39]</sup> such electric-field-induced control of magnetic spirals in the *P1* state does not rely on Dzyaloshinskii–Moriya interactions<sup>[40,41]</sup> (since, the  $J$  parameters of Figure 5d are extracted from Density functional theory (DFT) calculations where spin–orbit couplings (SOCs) are not taken into account).

### 3. Conclusions

In summary, properties of epitaxial (111) BFO films were investigated from first-principles. A rich variety of phases and phenomena are predicted in these systems. Examples include the sequence of *R3c* and two monoclinic phases (*Cc-I* and *Cc-II*) within the perovskite crystal structure when progressively increasing the tensile epitaxial strain. Another example is that these BFO films transform into another polymorph when further increasing their in-plane lattice constant, that is the hexagonal, YMnO<sub>3</sub>-type *P6<sub>3</sub>cm* phase. Strikingly, the out-of-plane polarization of this *P6<sub>3</sub>cm* state shows anomalous enhancement when strengthening the tensile epitaxial strain, as a result of the emergence of proper component of ferroelectricity—in addition to the “improper” one known to occur in other hexagonal systems.<sup>[13,14]</sup> Moreover, a magnetic transition resulting in the vanishing of the weak ferromagnetism, is also predicted when increasing  $a_{\text{IP}}$  within the stability region of the

YMnO<sub>3</sub>-type *P6<sub>3</sub>cm* state. Finally, for even larger in-plane lattice constants, the novel hex-like *P1* phase is found to be the ground state in epitaxial (111) BFO films. Motions of specific Fe ions in this hex-like *P1* phase results in the formation of original structural features (such as large Fe–O rings and 8-shaped Fe–O arrangements), as well as the creation of an in-plane polarization (in addition to an out of plane component), the existence of six energetically degenerate states and the occurrence of magnetic spirals. The magnitude and direction of the in-plane polarization and the period of the magnetic spirals are further found to strongly depend on the in-plane lattice parameter, which therefore allows a control and design of electric, magnetic, and magnetoelectric properties. Moreover, applying in-plane electric fields should allow BFO films to undergo a phase transition from one degenerate state to another degenerate hex-like *P1* state, which should also automatically change the propagation direction of the magnetic spirals and therefore constitute another original magnetoelectric effect. Our work therefore highlights epitaxial (111) multiferroics as a rich playground for novel phenomena. We hope that our predictions will be confirmed soon, especially since we also provide examples of substrates that can be used to observe our novel phases.

### 4. Experimental Section

**Density Functional Calculations and Analysis:** Density functional calculations were performed using the Vienna ab initio simulation package.<sup>[42]</sup> The generalized gradient approximation and the Perdew–Burke–Ernzerhof (PBE) functional for solid<sup>[43]</sup> were employed. A 500 eV plane wave cutoff energy was used for all calculations along with the projector augmented wave method,<sup>[44]</sup> with the Bi 6s and 6p electrons, Fe 3d and 4s electrons, and O 2s and 2p electrons being treated as valence states. An effective Hubbard  $U$  parameter of 4 eV was also employed to treat the 3d electrons of Fe ions.<sup>[14]</sup> Eleven phases were considered, with six of them being selected and presented here (see the other phases and the resulting whole phase diagram in the Supporting Information). Out of these six phases, three crystallize in the perovskite crystal structure, namely, a rhombohedral *R3c* and two monoclinic states that are denoted here as *Cc-I* and *Cc-II*; two others form hexagonal phases, and adopt the *P6<sub>3</sub>cm* and *P3<sub>2</sub>c1* space groups; and a (novel) phase of triclinic *P1* symmetry that can be thought as being derived from an hexagonal structure—which explains why it is denoted as “hex-like” in the text. The corresponding numbers of atoms in these phases were 30, 20, 20, 30, 30, and 30, respectively, and the  $k$ -point meshes were  $4 \times 4 \times 2$ ,  $4 \times 3 \times 3$ ,  $4 \times 3 \times 3$ ,  $4 \times 4 \times 2$ ,  $4 \times 4 \times 2$ , and  $4 \times 4 \times 2$ , respectively. The Hellman–Feynman forces were taken to be converged when they become smaller than  $0.001 \text{ eV \AA}^{-1}$  on each ion. The polarization was calculated using the modern (Berry-phase) theory of polarization<sup>[45]</sup> and further checked by computing the product between atomic displacements and Born effective charges. Phonon spectrums were calculated using the finite displacement method as implemented in the PHONOPY code,<sup>[46]</sup> with a single  $k$ -point at (0, 0, 0) and all axes of the supercell being longer than 10 Å. Phonon modes were then analyzed using the AMPLIMODES software.<sup>[47,48]</sup> Schematization of crystal structures were prepared using the VESTA software.<sup>[49]</sup>

**Determination of the Hex-like *P1* Phase:** The crystal structure of the hex-like *P1* phase was first discovered by soft modes analysis. More precisely, it was found that the zone-center  $\Gamma_2^-$  and some phonon modes at the  $K$  point (besides the so-called  $K_3$  mode) of the *P6<sub>3</sub>/mmc* phase become unstable when the in-plane lattice constants were larger than 6.40 Å. Following the eigenvectors of such unstable modes then leads to the stabilization of the *P1* phase. Note that a main consequence of the condensation of these phonon modes is that one of the Fe ions is

moving away from one of the equatorial oxygen ions, as shown in Figure 1f. The existence of this hex-like *P1* phase was then further confirmed by a genetic algorithm,<sup>[50]</sup> with the resulting atomic displacements being fully consistent with the atomic patterns associated with the aforementioned soft modes.

**Magnetism and Monte Carlo Simulations:** G-type AFM was employed for all the three studied perovskite phases, since it is known to be the magnetic ground state of (001) BFO films under strain.<sup>[6]</sup> When performing calculations that incorporate SOC and noncollinear magnetism, this G-type AFM vector was set to lie along the pseudocubic [1-10] direction, as found in some epitaxial (001) BFO films<sup>[6]</sup> (note that the direction of the AFM vector could change when varying the epitaxial strain, but the resulting energy differences were typically negligible as compared to those associated with structural phase transitions). Moreover, regarding the magnetism of the *P6<sub>3</sub>cm* and *P3<sub>2</sub>c1* phases, the symmetry allowed  $\Gamma_1$ ,  $\Gamma_2$ ,  $\Gamma_3$ , and  $\Gamma_4$  noncollinear, frustrated arrangements that are depicted in Figure 1 of ref. [14] were focused. Furthermore, the four-state method of ref. [51] is also employed within collinear DFT calculations, to determine the Heisenberg coupling coefficients specified in Figure 5 for a selected hex-like *P1* state (among the six degenerate ones). These coefficients were then used in Monte Carlo simulations<sup>[17]</sup> to search for low-energy magnetic structures. Magnetic energies were calculated for supercells ranging from  $1 \times 1 \times 1$  to  $20 \times 20 \times 1$  to determine the magnetic ground state configuration. In case of a spiral, the direction of its propagation, as well as its periodicity, was further checked by computing the spin structure factor<sup>[52]</sup>

$$S(\mathbf{q}) = \frac{1}{4N^2} \sum_{i,j} (\mathbf{S}_i \cdot \mathbf{S}_j) e^{i\mathbf{q}(\mathbf{r}_i - \mathbf{r}_j)} \quad (1)$$

where  $N$  is the number of spins,  $\mathbf{S}_i$  and  $\mathbf{S}_j$  are spin vectors and  $\mathbf{r}_i$  and  $\mathbf{r}_j$  are their real-space position, respectively. Note that the spin structure factor shows a peak at  $\mathbf{q}$ -point(s) of the Brillouin zone associated with the real-space spiral structure.

## Supporting Information

Supporting Information is available from the Wiley Online Library or from the author.

## Acknowledgements

The authors thank J. Íñiguez for useful discussion. This work was supported by the Office of Basic Energy Sciences under Contract No. ER-46612 (C.X. and H.X.), and by Air Force of Scientific Research under Grant No. FA9550-16-1-0065 (L.B.). H.X. was also supported by the NSFC (11374056), the Special Funds for Major State Basic Research (2015CB921700), Program for Professor of Special Appointment (Eastern Scholar), Qing Nian Ba Jian Program, and Fok Ying Tung Education Foundation. The Arkansas High Performance Computing Center (AHPCC) is also acknowledged for the use of its supercomputers.

## Conflict of Interest

The authors declare no conflict of interest.

## Keywords

(111) BiFeO<sub>3</sub>, tensile strains, novel phases, spin spiral, degenerate ferroelectric states

Received: July 23, 2017

Revised: August 7, 2017

Published online: September 28, 2017

- [1] Y. Tokura, *Science* **2006**, 312, 1481.
- [2] H. Schmid, *Ferroelectrics* **1994**, 162, 317.
- [3] G. Catalan, J. F. Scott, *Adv. Mater.* **2009**, 21, 2463.
- [4] T. Zhao, A. Scholl, F. Zavaliche, K. Lee, M. Barry, A. Doran, M. Cruz, Y. Chu, C. Ederer, N. Spaldin, R. R. Das, D. M. Kim, S. H. Baek, C. B. Eom, R. Ramesh, *Nat. Mater.* **2006**, 5, 823.
- [5] J. C. Wojdeł, J. Íñiguez, *Phys. Rev. Lett.* **2009**, 103, 267205.
- [6] D. Sando, A. Agbelele, D. Rahmedov, J. Liu, P. Rovillain, C. Toulouse, I. Infante, A. Pyatakov, S. Fusil, E. Jacquet, C. Carrétéro, C. Deranlot, S. Lisenkov, D. Wang, J.-M. Le Breton, M. Cazayous, A. Sacuto, J. Juraszek, A. K. Zvezdin, L. Bellaiche, B. Dkhil, A. Barthélémy, M. Bibes, *Nat. Mater.* **2013**, 12, 641.
- [7] Y. Yang, J. Íñiguez, A.-J. Mao, L. Bellaiche, *Phys. Rev. Lett.* **2014**, 112, 057202.
- [8] B. Xu, D. Wang, H. J. Zhao, J. Íñiguez, X. M. Chen, L. Bellaiche, *Adv. Funct. Mater.* **2015**, 25, 3626.
- [9] D. Kan, L. Pálóvá, V. Anbusathaiah, C.-J. Cheng, S. Fujino, V. Nagarajan, K. M. Rabe, I. Takeuchi, *Adv. Funct. Mater.* **2010**, 20, 1108.
- [10] Z. Chen, Z. Luo, C. Huang, Y. Qi, P. Yang, L. You, C. Hu, T. Wu, J. Wang, C. Gao, *Adv. Funct. Mater.* **2011**, 21, 133.
- [11] N. A. Spaldin, S.-W. Cheong, R. Ramesh, *Phys. Today* **2010**, 63, 38.
- [12] R. Zeches, M. Rossell, J. Zhang, A. Hatt, Q. He, C.-H. Yang, A. Kumar, C. Wang, A. Melville, C. Adamo, G. Sheng, Y.-H. Chu, J. F. Ihlefeld, R. Erni, C. Ederer, V. Gopalan, L. Q. Chen, D. G. Schlom, N. A. Spaldin, L. W. Martin, R. Ramesh, *Science* **2009**, 326, 977.
- [13] C. J. Fennie, K. M. Rabe, *Phys. Rev. B* **2005**, 72, 100103.
- [14] C. Xu, Y. Yang, S. Wang, W. Duan, B. Gu, L. Bellaiche, *Phys. Rev. B* **2014**, 89, 205122.
- [15] B. B. Van Aken, T. T. Palstra, A. Filippetti, N. A. Spaldin, *Nat. Mater.* **2004**, 3, 164.
- [16] N. Fujimura, T. Ishida, T. Yoshimura, T. Ito, *Appl. Phys. Lett.* **1996**, 69, 1011.
- [17] P. Wang, W. Ren, L. Bellaiche, H. Xiang, *Phys. Rev. Lett.* **2015**, 114, 147204.
- [18] H. J. Zhao, W. Ren, Y. Yang, J. Íñiguez, X. M. Chen, L. Bellaiche, *Nat. Commun.* **2014**, 5, 4021.
- [19] C. Xu, Y. Li, B. Xu, J. Íñiguez, W. Duan, L. Bellaiche, *Adv. Funct. Mater.* **2017**, 27, 1604513.
- [20] D. Puggioni, G. Giovannetti, M. Capone, J. M. Rondinelli, *Phys. Rev. Lett.* **2015**, 115, 087202.
- [21] J. A. Mundy, C. M. Brooks, M. E. Holtz, J. A. Moyer, H. Das, A. F. Rébola, J. T. Heron, J. D. Clarkson, S. M. Disseler, Z. Liu, A. Farhan, R. Held, R. Hovden, E. Padgett, Q. Mao, H. Paik, R. Misra, L. F. Kourkoutis, E. Arenholz, A. Scholl, J. A. Borchers, W. D. Ratcliff, R. Ramesh, C. J. Fennie, P. Schiffer, D. A. Muller, D. G. Schlom, *Nature* **2016**, 537, 523.
- [22] S. Bhattacharjee, E. Bousquet, P. Ghosez, *Phys. Rev. Lett.* **2009**, 102, 117602.
- [23] C. Ederer, N. A. Spaldin, *Phys. Rev. B* **2005**, 71, 224103.
- [24] H. Béa, B. Dupé, S. Fusil, R. Mattana, E. Jacquet, B. Warot-Fonrose, F. Wilhelm, A. Rogalev, S. Petit, V. Cros, A. Anane, F. Petroff, K. Bouzehouane, G. Geneste, B. Dkhil, S. Lisenkov, I. Ponomareva, L. Bellaiche, M. Bibes, A. Barthélémy, *Phys. Rev. Lett.* **2009**, 102, 217603.
- [25] S. Prosandeev, I. A. Kornev, L. Bellaiche, *Phys. Rev. B* **2011**, 83, 020102.
- [26] S. Prosandeev, I. A. Kornev, L. Bellaiche, *Phys. Rev. Lett.* **2010**, 105, 037208.
- [27] H. J. Zhao, Y. Yang, W. Ren, A.-J. Mao, X. M. Chen, L. Bellaiche, *J. Phys. Condens. Matter* **2014**, 26, 472201.
- [28] H. J. Zhao, C. Xu, Y. Yang, W. Duan, X. M. Chen, L. Bellaiche, *J. Phys. Condens. Matter* **2015**, 27, 485901.
- [29] X. Xu, W. Wang, *Mod. Phys. Lett. B* **2014**, 28, 1430008.



- [30] Diéguez, O. González-Vázquez, J. C. Wojdeł, J. Íñiguez, *Phys. Rev. B* **2011**, 83, 094105.
- [31] J. Bucci, B. Robertson, W. James, *J. Appl. Crystallogr.* **1972**, 5, 187.
- [32] H. Tan, C. Xu, M. Li, S. Wang, B.-L. Gu, W. Duan, *J. Phys. Condens. Matter* **2016**, 28, 126002.
- [33] H. M. Christen, J. H. Nam, H. S. Kim, A. J. Hatt, N. A. Spaldin, *Phys. Rev. B* **2011**, 83, 144107.
- [34] Lin, X. Wang, Y. Kamiya, G.-W. Chern, F. Fan, D. Fan, B. Casas, Y. Liu, V. Kiryukhin, W. H. Zurek, C. D. Batista, S.-W. Cheong, *Nat. Phys.* **2014**, 10, 970.
- [35] F.-T. Huang, S.-W. Cheong, *Nat. Rev. Mater.* **2017**, 2, 17004.
- [36] S. Bhattacharjee, D. Rahmedov, D. Wang, J. Íñiguez, L. Bellaiche, *Phys. Rev. Lett.* **2014**, 112, 147601.
- [37] D. Lebeugle, D. Colson, A. Forget, M. Viret, A. Bataille, A. Gukasov, *Phys. Rev. Lett.* **2008**, 100, 227602.
- [38] S. Lee, T. Choi, I. W. Ratcliff, R. Erwin, S. Cheong, V. Kiryukhin, *Phys. Rev. B* **2008**, 78, 100101.
- [39] D. Rahmedov, D. Wang, J. Íñiguez, L. Bellaiche, *Phys. Rev. Lett.* **2012**, 109, 037207.
- [40] I. Dzyaloshinskii, *Sov. Phys. JETP* **1964**, 19, 960.
- [41] T. Moriya, *Phys. Rev.* **1960**, 120, 91.
- [42] G. Kresse, D. Joubert, *Phys. Rev. B* **1999**, 59, 1758.
- [43] J. P. Perdew, A. Ruzsinszky, G. I. Csonka, O. A. Vydrov, G. E. Scuseria, L. A. Constantin, X. Zhou, K. Burke, *Phys. Rev. Lett.* **2008**, 100, 136406.
- [44] P. E. Blöchl, *Phys. Rev. B* **1994**, 50, 17953.
- [45] R. King-Smith, D. Vanderbilt, *Phys. Rev. B* **1993**, 47, 1651.
- [46] A. Togo, I. Tanaka, *Scr. Mater.* **2015**, 108, 1.
- [47] D. Orobengoa, C. Capillas, M. I. Aroyo, J. M. Perez-Mato, *J. Appl. Crystallogr.* **2009**, 42, 820.
- [48] J. Perez-Mato, D. Orobengoa, M. Aroyo, *Acta Crystallogr., Sect. A: Found. Crystallogr.* **2010**, 66, 558.
- [49] K. Momma, F. Izumi, *J. Appl. Crystallogr.* **2011**, 44, 1272.
- [50] X. Lu, X. Gong, H. Xiang, *Comput. Mater. Sci.* **2014**, 91, 310.
- [51] H. Xiang, E. Kan, S.-H. Wei, M.-H. Whangbo, X. Gong, *Phys. Rev. B* **2011**, 84, 224429.
- [52] J. W. Venderbos, M. Daghofer, J. van den Brink, S. Kumar, *Phys. Rev. Lett.* **2011**, 107, 076405.